Application of the Combined Feature Tracking and Maximum Cross-Correlation Algorithm to the Extraction of Sea Ice Motion Data From GF-3 Imagery

Mingci Li, Chunxia Zhou, Bing Li, Xiaoli Chen, Jianqiang Liu, and Tao Zeng

***Abstract*—In this study, an algorithm combining feature tracking and maximum cross-correlation (FT-MCC) for the extraction of sea ice motion (SIM) vectors were applied to Gaofen-3 (GF-3) imagery, filling the gap of SIM extraction using GF-3 imagery. The locally consistent flow field filtering method is proposed to replace the filtering method based on the correlation coefficient threshold in FT-MCC to improve filtering effectiveness of SIM results extracted by FT-MCC. A comparison of the probability density distributions (PDDs) of the correlation coefficients of SIM vectors extracted by FT-MCC from images with different resolutions revealed high reliability for SIM vectors extracted for images with an 80 m spatial resolution. A comparison of the PDDs of the correlation coefficients of SIM vectors obtained from images with different polarization modes showed more reliable SIM vectors were extracted from vertical transmit horizontal receive (VH) polarization images than from corresponding vertical transmit vertical receive (VV) polarization images. The SIM vectors extracted from GF-3 images by two methods (FT(A-KAZE)-MCC and FT(ORB)-MCC) derived from the FT-MCC algorithm were highly consistent in terms of accuracy and reliability. SIM vectors extracted manually and from Sentinel-1 images were used as reference data to verify the SIM results extracted from GF-3 images, for which the uncertainties in the magnitude and direction of the extracted SIM vectors were found to be 0.119 cm/s–0.287 cm/s (103 m/d–248 m/d) and 4.119°–5.930°, respectively.**

***Index Terms*—Correlation coefficient, feature tracking (FT), Gaofen-3 (GF-3), image information entropy, maximum cross-correlation (MCC), probability density distribution (PDD), sea ice motion (SIM).**

Manuscript received February 19, 2022; revised March 21, 2022; accepted April 8, 2022. Date of publication April 12, 2022; date of current version May 9, 2022. This work was supported in part by the National Key Research and Development Program of China under Grant 2018YFC1406102, in part by the Funds for the Distinguished Young Scientists of Hubei Province, China under Grant 2019CFA057, and in part by the National Natural Science Foundation of China (NSFC) under Grant 42171133, Grant 41941010, and Grant 41776200. *(Corresponding author: Chunxia Zhou.)*

Mingci Li, Chunxia Zhou, and Xiaoli Chen are with the Chinese Antarctic Center of Surveying and Mapping, Wuhan University, Wuhan 430079, China (e-mail: mingcich@whu.edu.cn; zhoucx@whu.edu.cn; zzuchenxiaoli@163.com).

Bing Li is with the School of Mathematics and Computer Science, Wuhan Polytechnic University, Wuhan 430048, China (e-mail: binglee@whpu.edu.cn).

Jianqiang Liu and Tao Zeng are with the National Satellite Ocean Application Service, Beijing 100081, China (e-mail: jqliu@mail.nsoas.org.cn; ztao10@mail.nsoas.org.cn).

This article has supplementary downloadable material available at https://doi.org/10.1109/JSTARS.2022.3166897, provided by the authors.

Digital Object Identifier 10.1109/JSTARS.2022.3166897

I. Introduction

GLOBAL warming has led to considerable changes in Arctic sea ice thickness and volume and multiyear ice coverage [1]. Sea ice motion (SIM) is both an important indicator for studying Arctic sea ice changes and a principal influence factor for the Arctic sea ice mass balance. In particular, the sea ice output from the Fram Strait has a significant impact on Arctic multiyear ice [2]–[4]. SIM is also a major factor affecting navigation safety in the Arctic. Therefore, studying SIM has considerable economic significance.

In recent decades, SIM data have been extracted from various types of remote sensing platforms, including passive microwave [5]–[7], radiometer [8], scatterometer [9], thermal infrared [10], [11], optical [12]–[14], and synthetic aperture radar (SAR) [15]–[20] imagery. These data are used to generate different types of SIM products. An increase in the number of data types used to extract SIM vectors has prompted the development of SIM extraction algorithms, among which maximum cross-correlation (MCC) and feature tracking (FT) are commonly used. MCC was the first algorithm used for the automated extraction of SIM vectors [11], which is realized by measuring the similarity between image blocks. MCC has the advantages of simple implementation and high robustness but also has several problems, for which some scholars have developed solutions. Continuous MCC [7], correlation coefficient fitting [21], and super-resolution [22] were subsequently developed to treat the quantization noise in SIM vectors extracted by MCC from low-resolution imagery, and parallel computing [23] and image pyramids [19] have been established to address the low computational efficiency of MCC. In addition, MCC has been used in combination with the Fourier-Mellin transform [24] to overcome its ineffectiveness at detecting the rotational motion of sea ice. FT algorithms implement SIM extraction by feature extraction and feature matching. ORB [25] and A-KAZE [26] are FT algorithms used in computer vision that have been successively applied for SIM extraction. FT algorithms produce independent SIM vectors and yield excellent results in the presence of sea ice rotation. However, the uneven distribution of the extracted SIM vectors makes sea ice deformation analysis and data assimilation challenging. Given these problems, an algorithm that combines the advantages of MCC and FT, referred to in this study as the FT-MCC algorithm,

This work is licensed under a Creative Commons Attribution-NonCommercial-NoDerivatives 4.0 License. For more information, see https://creativecommons.org/licenses/by-nc-nd/4.0/

TABLE I
INFORMATION FOR GF-3 AND SENTINEL-1 IMAGES

Satellite	Season	No.	Imaging date of Image 1 (YYYY-MM-DD | HH:MM:SS UTC)	Imaging date of Image 2 (YYYY-MM-DD | HH:MM:SS UTC)	Polarization mode	Time spans (day)	SIM speed range (cm/s)
GF-3	Winter	case1	2020-01-05 | 14:53:48	2020-01-11 | 14:05:46	VV + VH	6.0	1.3 - 1.8
		case2	2020-01-14 | 12:06:50	2020-01-16 | 12:23:59	VV + VH	2.0	8.4 - 10.7
		case3	2020-01-18 | 17:31:49	2020-01-19 | 18:30:16	VV + VH	1.0	0.1 - 2.9
	Summer	case4	2020-07-16 | 15:07:43	2020-07-18 | 13:45:23	VV + VH	1.9	0.0 - 6.3
Sentinel-1	Winter	case5	2020-01-05 | 14:35:43	2020-01-11 | 14:36:52	HH + HV	6.0	0.0 - 3.4
		case6	2020.01.18 | 16:52:26	2020.01.19 | 17:33:35	HH + HV	1.0	0.1 - 4.0
	Summer	case7	2020.07.16 | 16:54:35	2020.07.17 | 17:35:45	HH + HV	1.0	0.0 - 14.1

was developed [27], [28]. This algorithm can produce a grid-like distribution of SIM vectors and exhibits some versatility for detecting rotational motion of sea ice. FT-MCC has been used to extract SIM vectors from optical [14], C-band [27], [28], X-band [29] SAR images, and the fast ice identification [30].

Gaofen-3 (GF-3) was launched on August 10, 2016, and is China's first civilian C-band (5.3 GHz) multipolarization high-resolution SAR satellite with 12 imaging modes [31]–[33]. GF-3 imagery has been employed in multiple fields, such as ship identification [34], coastline extraction [35], sea surface wind field retrieval [36], sea ice identification [37], and sea ice classification [38]. However, there have been no reports on the using GF-3 imagery to obtain SIM data. In this study, FT-MCC was applied to GF-3 images to determine the prerequisites for obtaining high-reliability, high-accuracy results from this imagery. As FT-MCC was applied to GF-3 imagery for the first time in this study, the performance of two methods derived from this algorithm (see Section III-A-2 for details) were compared to identify the most suitable algorithm for extracting SIM data from GF-3 imagery. We verified the effectiveness of applying FT-MCC to GF-3 images for SIM vector extraction by comparing the results with SIM vectors extracted manually and from Sentinel-1 images.

The rest of this article is organized as follows. In Section II, GF-3 images, Sentinel-1 images, and the Copernicus Marine Environment Monitoring Service (CMEMS) SIM product used in this study are introduced. In Section III, the procedure for applying FT-MCC to GF-3 imagery is described in detail. In Section IV, the reliability and accuracy of the SIM vectors obtained from GF-3 images with different spatial resolutions and polarization modes are discussed, differences between SIM vectors extracted using the two methods based on FT-MCC are analyzed, and SIM vectors extracted from GF-3 are compared against those extracted manually and from Sentinel-1 images. Finally, Section V concludes this article.

II. DATA

A. GF-3 and Sentinel-1 Images

According to the coverage of GF-3 images in the Arctic, level-1A images acquired in Fine Stripe II (FSII) mode were selected as data sources for SIM extraction. These images had a resolution of 10 m, a swath width of 100 km, and selective dual-polarization. Considering that the time interval between image pairs used for SIM extraction and the speed of motion of sea ice in the covered area affect the results of SIM extraction [39]–[40], GF-3 image pairs were selected that were acquired for different time intervals, regions, and seasons. The location and acquisition time of the selected GF-3 images are shown in Table I and Fig. 1.

The quality of the SIM vectors extracted from GF-3 images was assessed by comparison against SIM vectors extracted from Sentinel-1 images. Based on previous studies on SIM vector extraction from Sentinel-1 imagery [25]–[28], Sentinel-1 ground-range images acquired in extra wide mode with a resolution of 40 m were used in this study. Table I and Fig. 1 provide the information and locations of the Sentinel-1 images.

B. CMEMS SIM Products

To ensure the reliability of the SIM results extracted from Sentinel-1 imagery, we used the high resolution near real time single swath data from CMEMS as reference data. The SIM products from CMEMS were obtained from SAR imagery using the MCC method by the Technical University of Denmark with a spatial resolution of 10 km and a temporal resolution of approximately 1 day [41].

III. METHODS

A. FT-MCC

FT-MCC was used to extract SIM vectors. The main procedure of the algorithm is described in the following.

1) A SAR image is preprocessed to produce a grayscale image with gray values in the range of [0, 255].
2) FT is performed to yield nonuniformly distributed SIM vectors.
3) Linear and polynomial interpolation are performed to estimate the SIM vectors on a regular grid.
4) MCC is performed to refine the estimated SIM vectors on a regular grid.
5) Filtering is performed to remove erroneous SIM vectors.

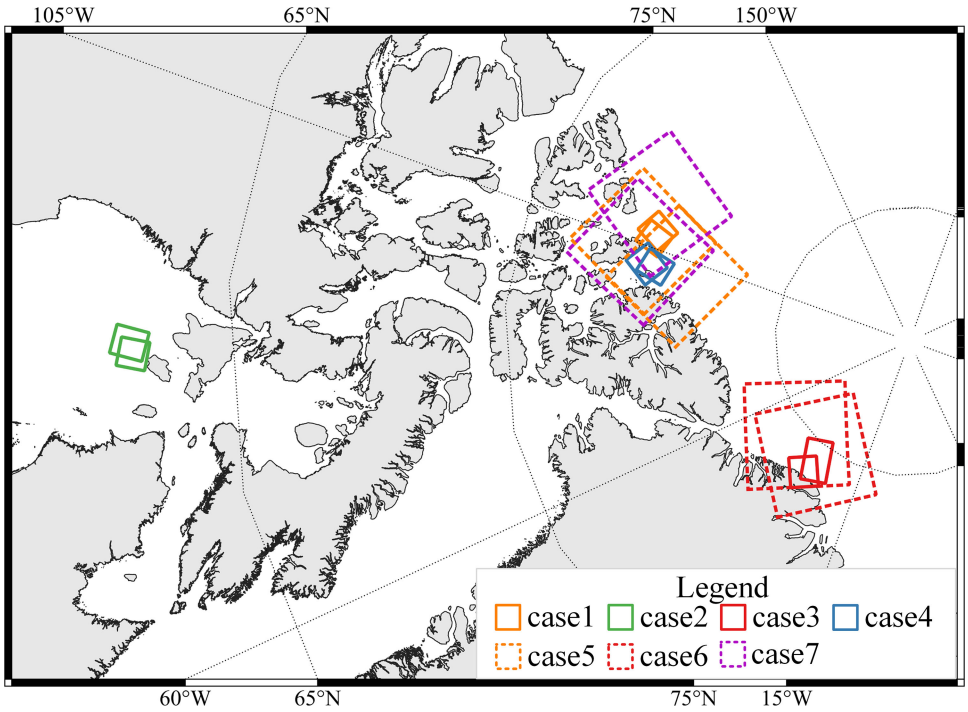

Fig. 1. Locations and coverage of the images used in this study.

The FT-MCC method reported in the literature [27], [28] was modified in this study by replacing the filtering method based on the correlation coefficient threshold (CCT) in Step 5 with a locally consistent (LC) flow field filtering method. The replacement scheme effectively eliminates incorrect vectors while retaining correct vectors with small correlation coefficients, and the detailed procedure is described in Section III-A-5.

1) Data Preprocessing: A level-1A GF-3 image in FSII mode was single-look complex (SLC) image, which needs to be transformed into a grayscale image with gray values ranging from 0 to 255 through the following procedure.

a) Radiation correction: Equation (1) was used to perform radiation correction on GF-3 images [32]. A backscatter coefficient was obtained for each pixel

$$\sigma^0 = 10\log_{10}\frac{(I^2+Q^2)*qv^2}{32767^2} - K \tag{1}$$

where σ^0 is the corrected backscatter coefficient; I and Q are the real and imaginary parts of the SLC image, respectively; and qv and K are the quality value and calibration constant, respectively, which were obtained from the metadata contained in the image.

b) Multilook processing and speckle filtering: Multilook processing can be used to acquire images at a specified resolution while suppressing speckle noise in images. In this study, the spatial domain average method (Fig. 2) was used for multilook processing. Firstly, the size of the spatial sampling window is calculated based on the resolutions of the target and SLC images; then the radiation-corrected image is divided into a grid according to the size of the spatial sampling window, and the average backscattering coefficient in each window is calculated to obtain a multilook processed image.

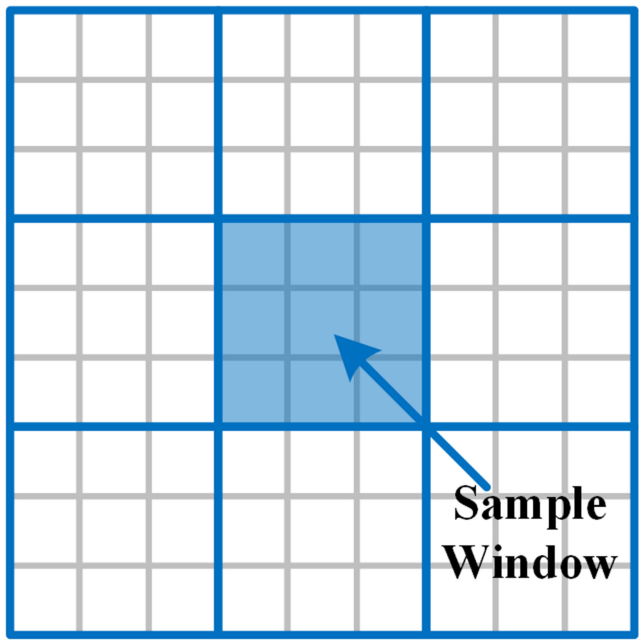

Fig. 2. Schematic of the spatial domain average method. The gray grids represent radiation-corrected images, and the blue grids represent the images after multilook processing.

To further reduce the effects of speckle noise on FT-MCC, Lee filtering [43] was performed on the images after multilook processing. Lee filtering is a typical method that filters speckles in SAR images based on their local statistical properties and is effective at reducing the effects of speckle noise.

c) Regularization: The filtered σ^0 image in this study was regularized through percentage truncation and stretching based

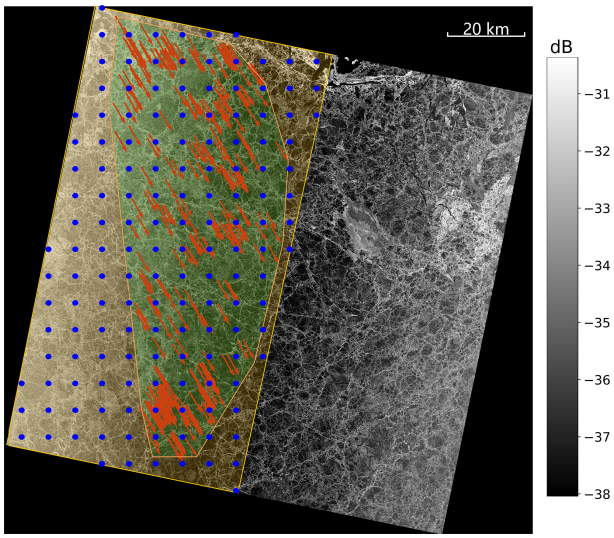

Fig. 3. SIM vector estimation on a regular grid. The red arrows signify indicate the SIM vectors obtained through FT, the blue dots indicate the start points of the estimated SIM vectors on the grid, the green area shows the range of the nonuniformly distributed SIM vectors obtained through FT, and the union of the orange and green areas indicates the overlap of the two images used to extract the SIM vectors.

on the following equation:

$$i = 255 \cdot \frac{\sigma^0 - \sigma^0_{\min}}{\sigma^0_{\max} - \sigma^0_{\min}} \tag{2}$$

where $\sigma^0_{\min}$ and $\sigma^0_{\max}$ are the 10th and 99th percentiles of σ^0, respectively.

d) Reprojection: Based on its rational polynomial coefficient, the regularized grayscale image was projected to the WGS-84/National Snow and Ice Data Center Sea Ice Polar Stereographic North coordinate system.

2) FT: Based on previous studies on the SIM vector extraction from C-band Sentinel-1 imagery, two algorithms, A-KAZE and ORB, were used for FT. The FT-MCC algorithms that track features using A-KAZE and ORB are referred to as the FT(A-KAZE)-MCC and FT(ORB)-MCC algorithms, respectively; please refer to [25] and [26] for the FT procedures of ORB and A-KAZE, respectively.

To reduce the impact of potentially erroneous vectors on subsequent steps, the FT results were filtered using the least-squares method [27].

3) Estimation of the SIM Vectors on a Regular Grid: The grid-like distribution of the SIM vectors was estimated in this study based on nonuniformly distributed SIM vectors obtained through FT. There were two scenarios in the estimation process. First, the start point (each blue dot in Fig. 3) of the estimated vector was within the range of the SIM vectors obtained through FT (the green area in Fig. 3). Second, the start point (each blue point in Fig. 3) of the estimated vector was outside the range of the SIM vectors obtained through FT (the orange area in Fig. 3). Linear and polynomial interpolation were used for scenarios 1 and 2, respectively. Muckenhuber and Sandven [27] provided detailed procedures of these two estimation methods.

4) MCC: There are deviations between the estimated SIM vectors of the gridded distribution and the real SIM vectors, and

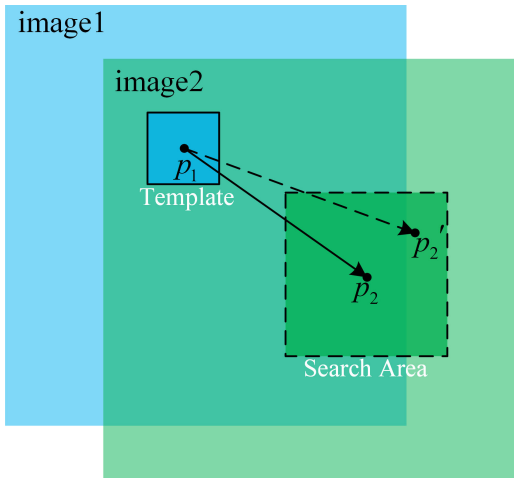

Fig. 4. MCC-based refinement of an estimated motion vector. p_1 and p_2 are the start and end points of the estimated vector, respectively. p_2' is the refined p_2, p_1 and p_2' are the start and end points of the refined vector, respectively.

the MCC is needed to refine the estimated motion vectors. For the MCC, the correlation coefficient ρ is calculated using the following equation:

$$\rho = \frac{\sum_{i,j}(a_{ij} - \bar{a})(b_{ij} - \bar{b})}{\sqrt{\sum_{i,j}(a_{ij} - \bar{a})^2 \sum_{i,j}(b_{ij} - \bar{b})^2}} \tag{3}$$

where a is the matching template in image 1, and b is a subset (as large as a) within the search area in image 2. Considering the effects of sea ice rotation on MCC, the matching templates are rotated by a specified angle within an angle range to obtain a set of matching templates $[T_1, T_2, \ldots, T_n]$. The set of maximum correlation coefficients $[\rho_1, \rho_2, \ldots, \rho_n]$and set of positions $[(x_1, y_1), (x_2, y_2), \ldots, (x_n, y_n)]$ are obtained by locating the position with the maximum correlation coefficient for each matching template T_i in the search area of image 2 (Fig. 4). The maximum correlation coefficient $\rho_{i\max}$ in $[\rho_1, \rho_2, \ldots, \rho_n]$ and the corresponding position $(x_i, y_i)_{\max}$, where $(x_i, y_i)_{\max}$ is the final refined position, are calculated.

5) Filtering of SIM Vectors: The LC flow field filtering procedure was used in this study to eliminate erroneous SIM vectors and is described in the following.

1) LC filtering is performed in the x-direction by calculating the absolute difference between the velocity of each SIM vector and the mean velocity of the neighboring SIM vectors in the x-direction. If the difference exceeds a specified threshold, the vector is removed.
2) The same method used for LC filtering in the x-direction is used for the y-direction.
3) SIM vectors with fewer than four neighboring SIM vectors are removed [43].

An adaptive filtering threshold is used for LC filtering in the x- and y-directions to accommodate different data. The absolute difference between the velocity of each vector and the mean velocity of its neighboring vectors is first calculated. Then, the filtering threshold is set to 1.5 times the standard deviation (SD) of the absolute differences.

B. Selection of GF-3 Image Parameters

In this study, VH- and VV-polarized images with resolutions of 20, 40, 60, 80, and 100 m for GF-3 FSII mode obtained after the data preprocessing procedure described in Section III-A-1 were used. The FT-MCC algorithm was used to extract SIM data from images with different resolutions and polarization modes. The results were compared in terms of reliability to determine the image resolution and polarization mode suitable for SIM vector extraction. The reliability of the extracted SIM data was evaluated through the calculation of the probability density distribution (PDD) of the ρ values of the SIM vectors. The value of ρ corresponding to the peak probability density, $\rho_{\max}$, was calculated. High $\rho_{\max}$ values suggest high reliability in the extracted SIM data.

C. Accuracy Assessment and Comparison

The accuracy of the SIM vectors extracted from the GF-3 images was evaluated against reference data. The means and SDs of the absolute differences in the velocity magnitude and velocity direction were used as the metrics to examine the accuracy.

The start positions of the reference vectors and the vectors extracted from the GF-3 images are different and must be matched. The nearest neighbor method was used for pairing. The criteria of this method are as follows: the distance between the start point of a reference SIM vector and that of an SIM vector extracted from the GF-3 images was the nearest possible and did not exceed $\sqrt{2}/2$ times the spatial resolution of the extracted SIM vector, and there were no fewer than four effective vectors in the vicinity of each of the start and end points of a reference vector [43].

IV. Results and Discussion

A. Effectiveness of LC Filtering

The effectiveness of CCT method for SIM vector fields depends on the selected threshold, which must be adjusted for the season in which images are acquired. In winter (summer), the small (large) feature variation of sea ice in SAR images generally results in large (small) correlation coefficients for the obtained SIM vectors, such that a high (low) threshold must be set to eliminate incorrect vectors. To circumvent threshold value selection for CCT method, we applied LC flow field filtering method to filter the SIM vectors, and the results are shown in Fig. 5 and Fig. S1. Using CCT method with a threshold of 0.2 produces many incorrect vectors. Increasing the threshold to 0.4 eliminates more correct vectors. However, using the LC flow field filtering method, retains a large number of correct vectors with low correlation coefficients, while eliminating incorrect vectors.

B. Comparison of Results Extracted From Images With Different Resolutions

The speckle noise in SAR images affects the reliability of FT-MCC for SIM vector extraction. Both multilook processing (reducing image resolution) and Lee filtering can be used for image preprocessing to suppress the speckle noise in images. In this study, the equivalent number of looks (ENL) was used to compare the level of speckle noise suppression by multilook processing and Lee filtering. Fig. 6 shows the results, where a large ENL indicates a low level of speckle noise.

Fig. 6 shows that reducing the image resolution suppresses speckle noise more effectively than Lee filtering. Considering the effect of different filter kernels and the size of the filter kernel on the Lee filtering efficiency (Fig. S2), a 7×7 filter kernel was selected. The trend in the ENL with the image resolution shows that the speckle noise cannot be significantly reduced below a well-defined image resolution.

To select an appropriate image resolution for SIM extraction, FT(A-KAZE)-MCC and FT(ORB)-MCC were used to extract SIM vectors from preprocessed GF-3 images with different spatial resolutions. Then, the PDDs of the ρ values of the SIM vectors were calculated (Fig. 7).

Fig. 7 shows that the SIM vectors obtained from the FSII mode images with a resolution of 20 m had ρ values concentrated at approximately 0.2, suggesting low reliability in these SIM vectors. Similar PDD trends were observed for the ρ values of SIM vectors obtained from images with resolutions of 40, 60, 80, and 100 m, although the ρ values of the SIM vectors obtained from the 80 m resolution images appear slightly more frequently in the range of 0.85–0.9 than those for images with other resolutions.

Considering the results for the speckle noise level in images with different resolutions (Fig. 6) together with the PDDs of the ρ values of SIM vectors (Fig. 7) shows that the poor reliability of the extracted SIM vectors from the FSII mode 20 m resolution images is mainly due to high speckle noise in these images. Based on the aforementioned results, GF-3 images with an 80 m resolution in FSII mode were selected for SIM extraction in this study.

C. Comparison of Results Obtained From VH- and VV-Polarized Images

FT(A-KAZE)-MCC and FT(ORB)-MCC were used to extract the SIM vectors from GF-3 images in summer and winter, respectively. Subsequently, the PDDs of the ρ values of the SIM vectors were calculated (Fig. 8).

Fig. 8 reveals the following. For the FSII mode images acquired in summer, the SIM vectors extracted from the VH-polarized images were more likely to have large ρ values than those obtained from the VV-polarized images, suggesting higher reliability in the SIM vectors extracted from the VH-polarized images than those extracted from the VV-polarized images. The SIM vectors extracted from the FSII mode VH- and VV-polarized images acquired in winter displayed highly similar PDD patterns, with those extracted from the VH-polarized images being slightly more likely to have ρ values in the range of 0.85–0.9 than those extracted from the VV-polarized images, suggesting that the reliability of the SIM vectors extracted from the VH-polarized images acquired in winter was only slightly higher than that of the SIM vectors extracted from the VV-polarized images acquired in winter.

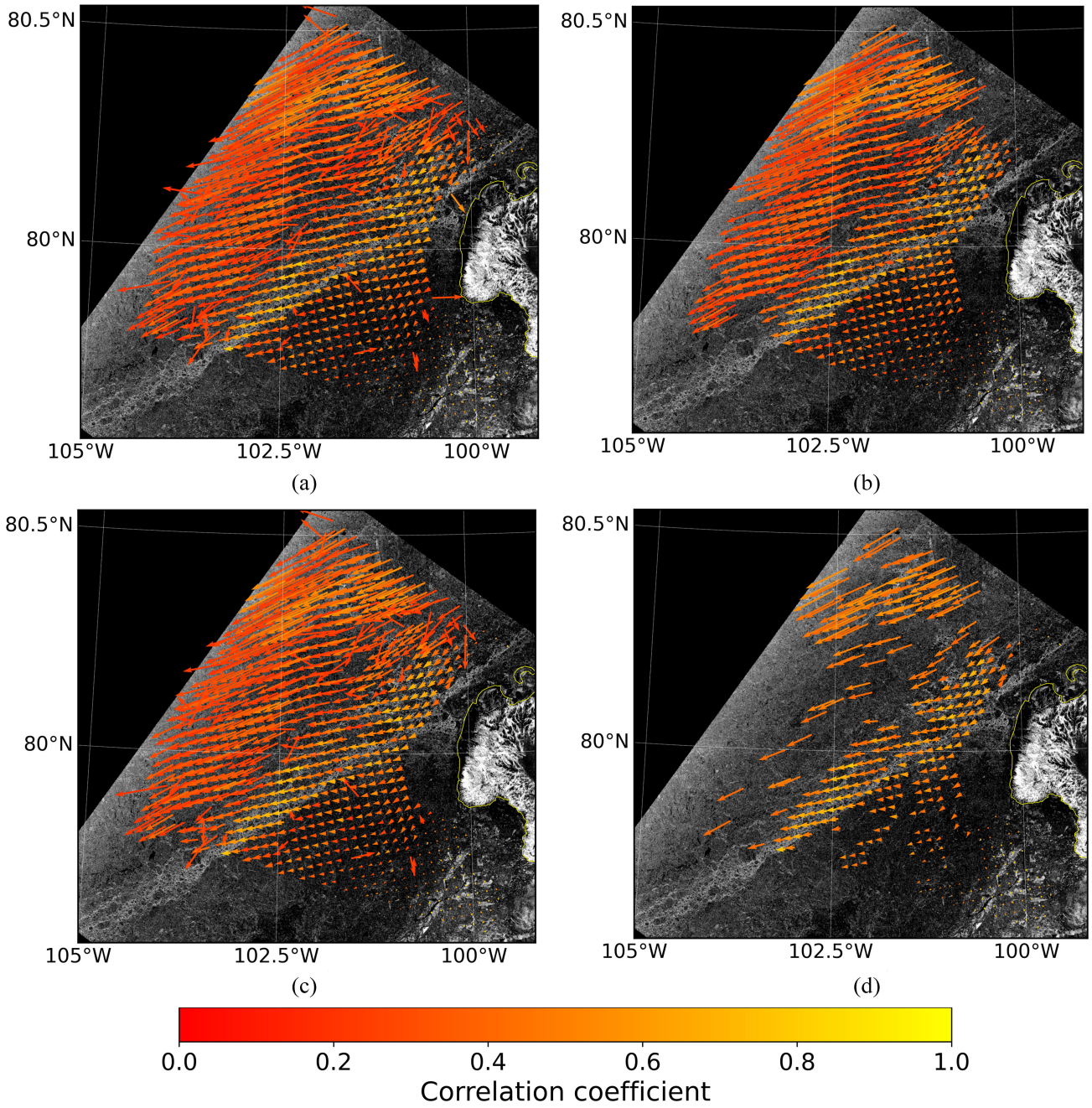

Fig. 5. Comparison of filtered results. (a) Unfiltered SIM vector field. (b) Result obtained by LC flow field filtering; results obtained using CCT with thresholds of (c) 0.2 and (d) 0.4.

The rich grayscale information of images can increase the identifiability of sea ice features and thus affect the reliability of SIM vectors. In this study, we chose the information entropy [44], which is insensitive to noise, to evaluate the richness of grayscale information in images [45], and the image information entropy is defined as follows:

$$H(x) = -\sum_{i=0}^{255} p_i(x) \log p_i(x) \tag{4}$$

where $p_i(x)$ is the frequency of grayscale i in the image, and a large $H(x)$ indicates rich grayscale information in the image.

Fig. 9 shows the information entropy calculated for the VH- and VV-polarized images with an 80 m resolution acquired in FSII mode. The VH-polarized images acquired in FSII mode in the winter have a higher mean information entropy and therefore richer grayscale information than the corresponding VV-polarized images. Similar results are obtained for the summer images. The characteristics of the information entropy of the VH- and VV-polarized images are consistent with the reliability of the corresponding extracted SIM, suggesting that the rich grayscale information in the images is responsible for the higher reliability of the SIM data obtained from the FSII mode VH-polarized images.

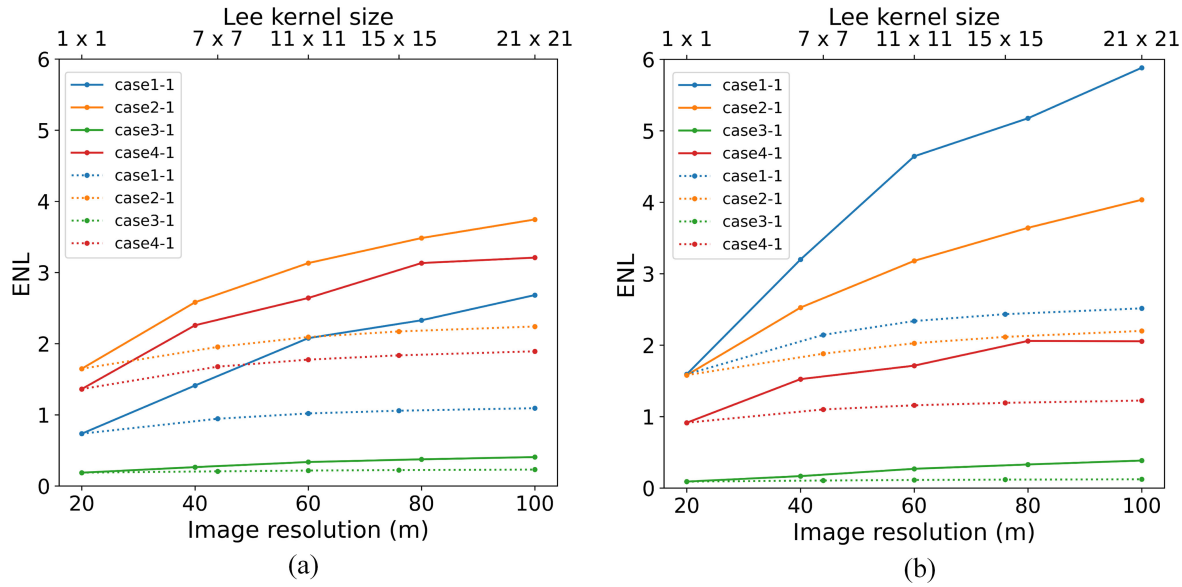

Fig. 6. Effect of the image resolution (solid lines) and Lee filter kernel size (dashed lines) on the ENL for (a) VH-polarized and (b) VV-polarized images acquired in FSII mode.

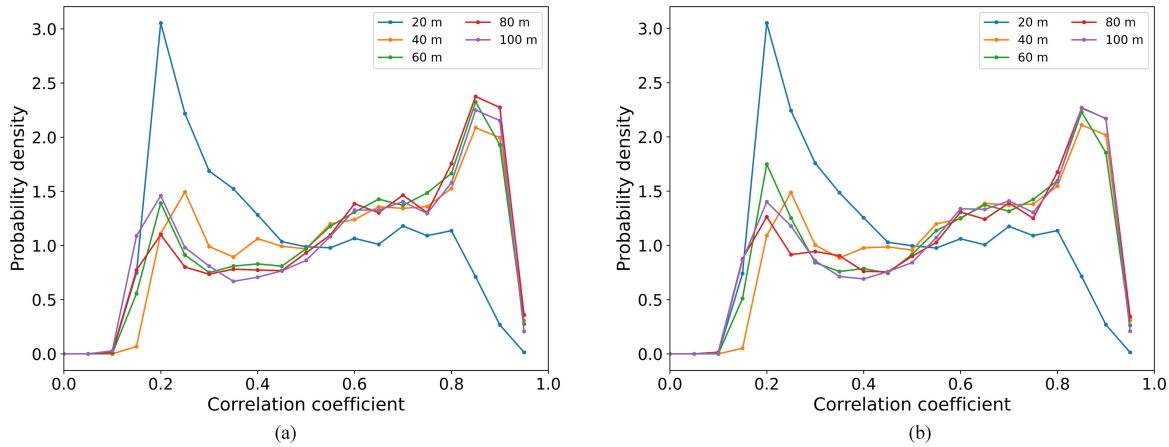

Fig. 7. PDDs of the ρ values of the SIM vectors for FSII mode images with different spatial resolutions obtained using (a) FT(A-KAZE)-MCC and (b) FT(ORB)-MCC. The number of SIM vectors is the sum of the number of SIM vectors obtained from the four pairs of FSII VH- and VV-polarized images presented in Table I.

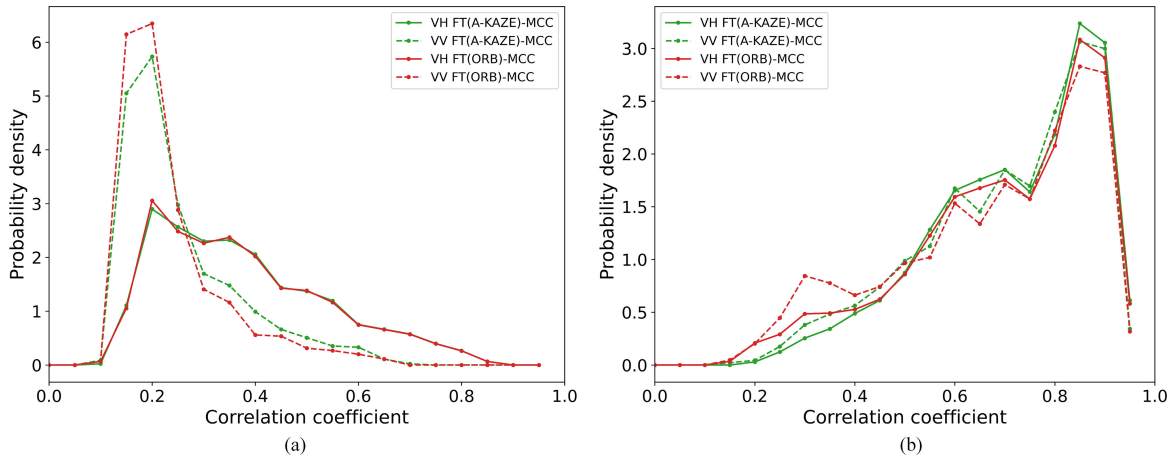

Fig. 8. PDDs of the ρ values of the SIM vectors extracted from the GF-3 VH- and VV-polarized 80 m resolution FSII mode images presented in Table I acquired in the (a) summer and (b) winter.

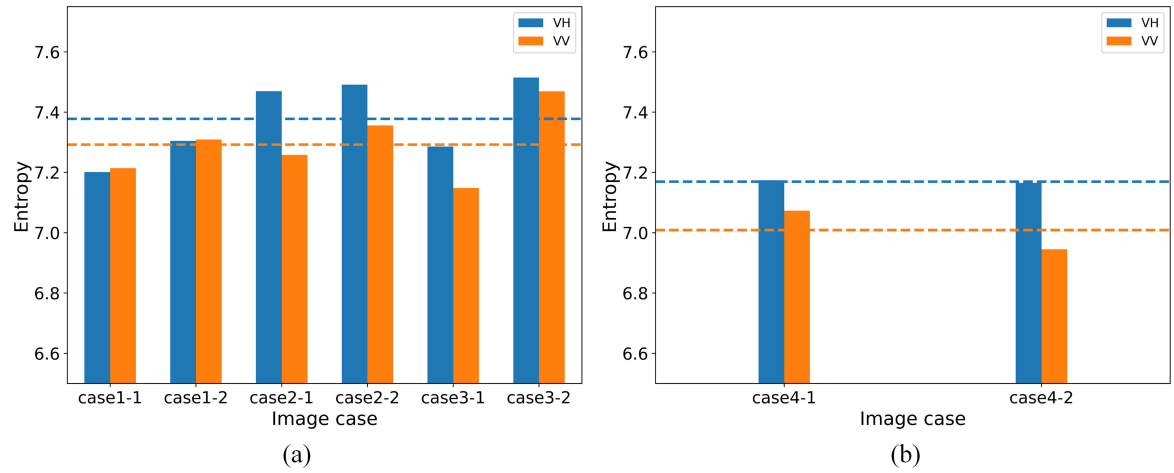

Fig. 9. Information entropy of VH- and VV-polarized images acquired in FSII mode in the (a) winter and (b) summer. The blue and orange dashed lines indicate the mean information entropy of the VH- and VV-polarized images, respectively.

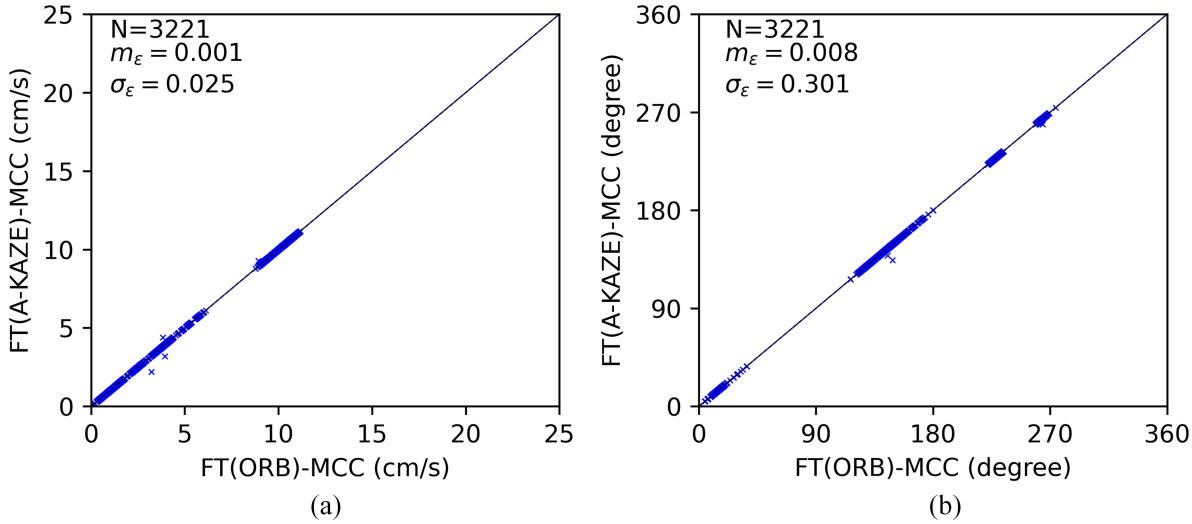

Fig. 10. Comparison of the magnitude and direction of SIM vectors extracted by FT(A-KAZE)-MCC and FT(ORB)-MCC. The number of vectors compared, N, is the sum of the number of SIM vectors obtained from the four pairs of GF-3 images presented in Table I. m_ε and σ_ε are the mean and SD of the absolute difference in the magnitude or direction of the extracted SIM vectors, respectively.

D. Comparison of FT(A-KAZE)-MCC and FT(ORB)-MCC

FT(A-KAZE)-MCC and FT(ORB)-MCC were used to extract SIM vectors from GF-3 images. Fig. 10 is a comparison of the magnitude and direction of the obtained SIM vectors. The SDs of the absolute difference in the magnitude and direction of the SIM vectors obtained using the two methods are 0.025 cm/s (21.6 m/d) and 0.301°, respectively. The magnitude and direction of the SIM vectors obtained by the two methods are highly consistent.

Fig. 11 shows the PDDs of the ρ values of the two methods were highly consistent. Considering both the PDDs of the ρ values and the absolute difference in the magnitude and direction of the SIM vectors of the two methods, it is concluded that the SIM vectors obtained by the two methods on the GF-3 images show high consistency.

Table II shows that FT(A-KAZE)-MCC is significantly more efficient than FT(ORB)-MCC. Comparing the efficiency of

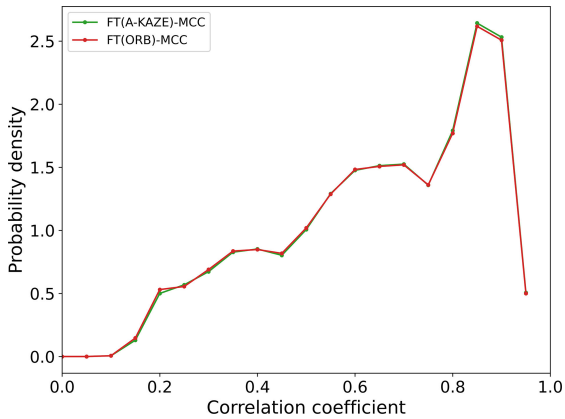

Fig. 11. PDDs of the ρ values of the SIM vectors obtained by the FT(A-KAZE)-MCC and FT(ORB)-MCC. The number of SIM vectors is the sum of the number of SIM vectors obtained from the four pairs of GF-3 images presented in Table I.

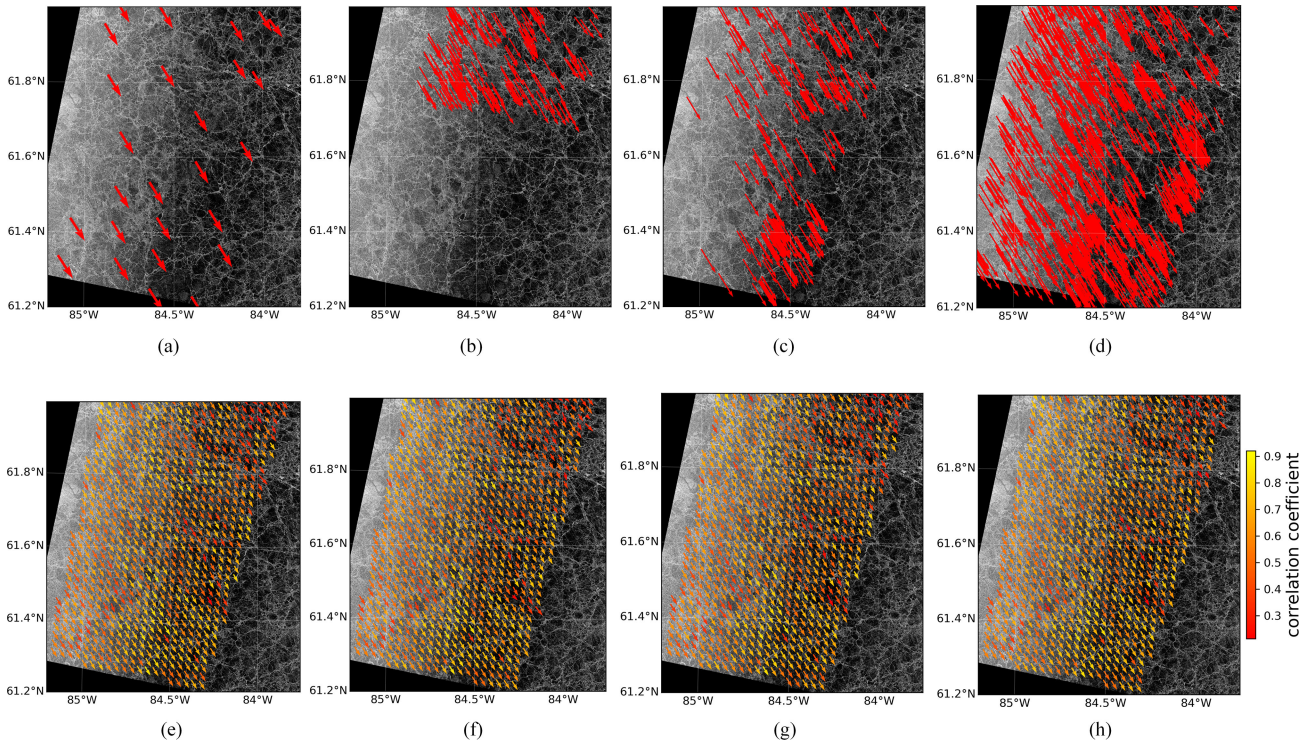

Fig. 12. Impact of the number of SIM vectors obtained through FT on the output of the FT-MCC algorithm. (a)–(d) Distributions of the different numbers (26, 197, 401, and 1436, respectively) of SIM vectors obtained through FT. (e)–(h) Grid-like distributions of the SIM vectors yielded by the subsequent process based on the results in (a)–(d), respectively.

TABLE II
COMPARISON OF EFFICIENCIES OF FT(A-KAZE)-MCC AND FT(ORB)-MCC IN UNITS OF SECONDS

		case1	case2	case3	case4
FT(A-KAZE)-MCC	A-KAZE	1.788	3.146	2.876	1.250
	MCC	1.028	1.383	1.338	1.252
FT(ORB)-MCC	ORB	22.415	34.020	26.548	17.145
	MCC	1.442	1.655	1.885	1.373

different stages of the two methods showed that A-KAZE was more efficient than ORB, which is the reason for the higher efficiency of FT(A-KAZE)-MCC.

Demchev *et al.* [26] compared the SIM vectors extracted by two FT algorithms, A-KAZE and ORB, from Sentinel-1 imagery and noted that A-KAZE was superior to ORB in terms of their extraction of SIM vectors. On this basis, we believe that the results produced by the FT(A-KAZE)-MCC algorithm should be better than those produced by the FT(ORB)-MCC algorithm. However, the comparative analysis presented earlier shows these two algorithms yielded highly consistent SIM vectors from GF-3 images, albeit with different efficiencies. This discrepancy can be attributed to the fact that in FT-MCC, the results obtained through FT were only used to estimate SIM vectors at the regular grid, which was subsequently used to reduce the matching area for MCC and accelerate the MCC process. As a result, the number of SIM vectors obtained through FT did not have a significant impact on the final output of the FT-MCC algorithm.

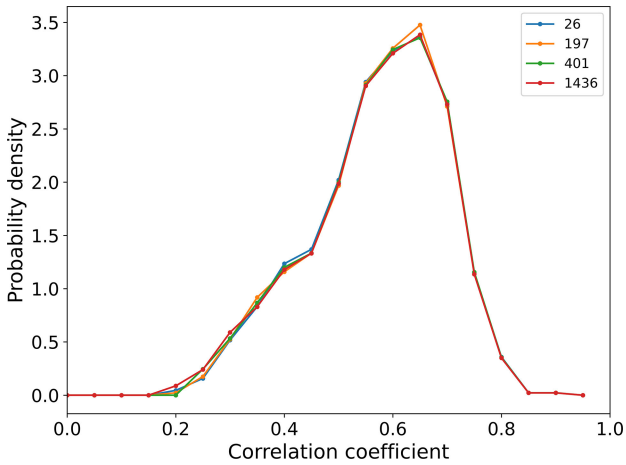

Fig. 13. Impact of the number of SIM vectors obtained through FT on the distribution of the ρ values of the SIM vectors yielded by the FT-MCC algorithm.

The different numbers of SIM vectors obtained through FT were used to perform the subsequent steps of the FT-MCC algorithm to examine the impact of the number of SIM vectors obtained through FT on the output of the FT-MCC algorithm.

As shown in Fig. 12, the SIM vectors on the regular grid obtained based on different numbers of SIM vectors obtained through FT displayed consistent spatial distribution patterns. Statistical analysis (Fig. 13) revealed that the ρ values of the SIM vectors in the four distributed grids in Fig. 12 (e)–(h) were almost identical. Figs. 12 and 13 show that the SIM vectors obtained

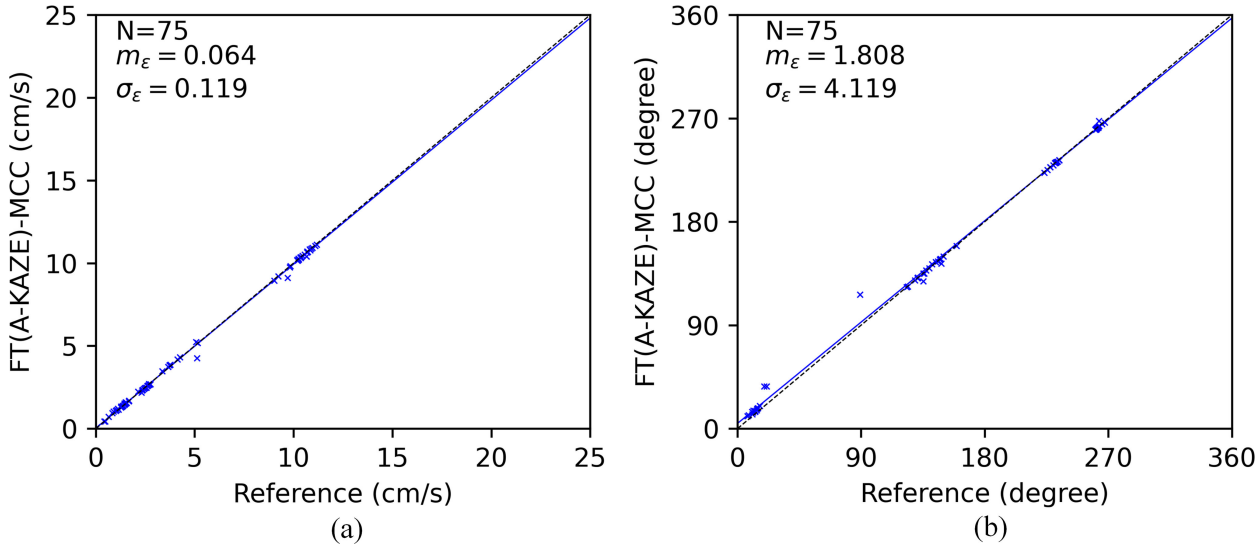

Fig. 14. Assessment of the accuracy of extracted results using manually extracted SIM vectors as reference data. (a) and (b) Assessment results for the magnitude and direction, respectively, of SIM vectors extracted from a GF-3 image. N is the number of automatically (FT(A-KAZE)-MCC) and manually (reference) extracted vector pairs. m_ε and σ_ε are the mean and SD, respectively, of the absolute deviation of the magnitude or direction of the SIM vectors extracted manually and automatically. The SIM vectors assessed in the figure are the set of results extracted from all the GF-3 image pairs presented in Table I. The blue dashed line is a least-squares linear fit to the blue scatter points.

through FT from the GF-3 images did not have a significant impact on the final grid-like distribution of the SIM vectors yielded by the FT-MCC algorithm and that the SIM vectors extracted by the FT(A-KAZE)-MCC and FT(ORB)-MCC algorithms from the GF-3 images were consistent.

E. Accuracy Assessment

Based on the results presented in the previous section, we used FT(A-KAZE)-MCC to extract SIM vectors from the GF-3 FSII mode VH-polarized 80 m resolution image.

The accuracy of the extracted SIM vectors was assessed by the method described in Section III-C using two independent datasets: SIM data manually extracted from GF-3 images and SIM data extracted from Sentinel-1 images by the method in [27]. We did not directly assess the SIM vectors extracted from GF-3 imagery using currently released SIM products because the temporal resolution of these products does not match that of the SIM data extracted from GF-3 and SIM vectors extracted from SAR imagery are generally considered more accurate than those extracted from low-resolution passive microwave data [46]. Thus, we first selected the CMEMS SIM products extracted from SAR images to assess the SIM vectors extracted from Sentinel-1 images to ensure their reliability as reference data, and then used the SIM data extracted from the Sentinel-1 images to evaluate the SIM data extracted from the GF-3 images.

1) Using Manually Extracted SIM Vectors as Reference Data: The accuracy of the SIM vectors extracted from the GF-3 images was investigated using manually extracted SIM vectors as reference data. Fig. 14 and Fig. S3 show that the SIM vectors extracted from a GF-3 image by FT(A-KAZE)-MCC had high accuracy. The uncertainties of the SIM speeds were 0.119 cm/s (103 m/day), and the uncertainties of the SIM directions were 4.119°.

2) Using SIM Vectors Extracted From Sentinel-1 Images as Reference Data: Considering that the temporal resolution of CMEMS SIM products is approximately 1 day, the image pairs case6 and case7 in Table I with a time interval of approximately 1 day were assessed, and the results are shown in Fig. 15. The SDs of the absolute difference of the SIM vectors magnitude extracted from the Sentinel-1 image and the magnitude of CMEMS SIM vectors is 0.224 cm/s (193 m/d), and the SD of the absolute difference of the direction is 4.179°, which is considered to be a better consistency of the two SIM data.

The GF-3 image pairs and Sentinel-1 image pairs (case1 and case5, case3, and case6) with close in time were selected. The SIM vectors extracted from Sentinel-1 images were used as reference data to assess the accuracy of the SIM vectors extracted from GF-3 images. The results are shown in Fig. 16. The SIM vectors extracted from the GF-3 and Sentinel-1 images are generally consistent, with SDs of 0.180 cm/s (155 m/d) and 4.207° for the absolute difference in the magnitude and direction of the velocity, respectively.

Combining the assessment results in Figs. 15 and 16 with the error propagation [47], the SDs of the absolute difference of the velocity magnitude between the CMEMS SIM product and the SIM data extracted from GF-3 are calculated according to (5) is 0.287 cm/s (248 m/d), and the SD of the absolute difference of the velocity direction is 5.930°.

$$\sigma^2_{CMEMS\_GF3} = \sigma^2_{CMEMS\_S1} + \sigma^2_{S1\_GF3}. \tag{5}$$

Comparing the assessment results of two independent datasets on the accuracy of SIM vectors extracted from GF-3 images, showed that the accuracy of SIM vectors extracted from the GF-3 images was underestimated when using the Sentinel-1 extraction vectors as reference data because the times of the Sentinel-1 and GF-3 image pairs did not coincide. In addition, due to the limited number of manually extracted SIM vectors, the accuracy

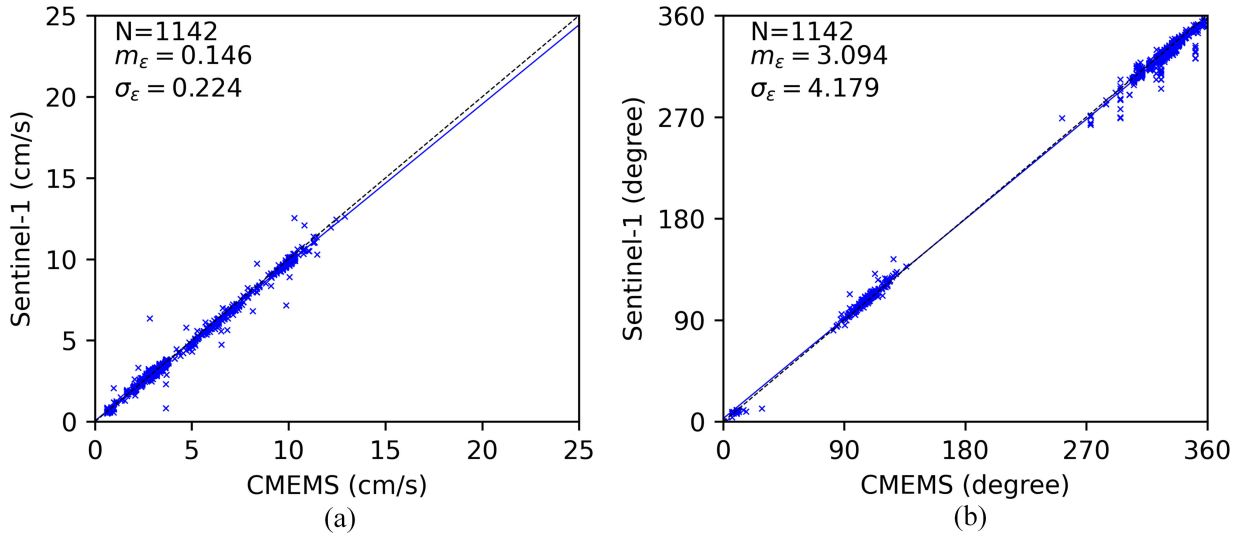

Fig. 15. Reliability of SIM vector extraction from Sentinel-1 images is assessed using CMEMS SIM products. (a) and (b) Assessment results for the magnitude and direction, respectively, of SIM vectors extracted from Sentinel-1 images. The blue dashed line is a least-squares linear fit to the blue scatter points. N is the number of Sentinel-1 and CMEMS SIM vector pairs. m_ε and σ_ε are the mean and SD, respectively, of the absolute deviation of the magnitude or direction of the SIM vectors from Sentinel-1 and CMEMS.

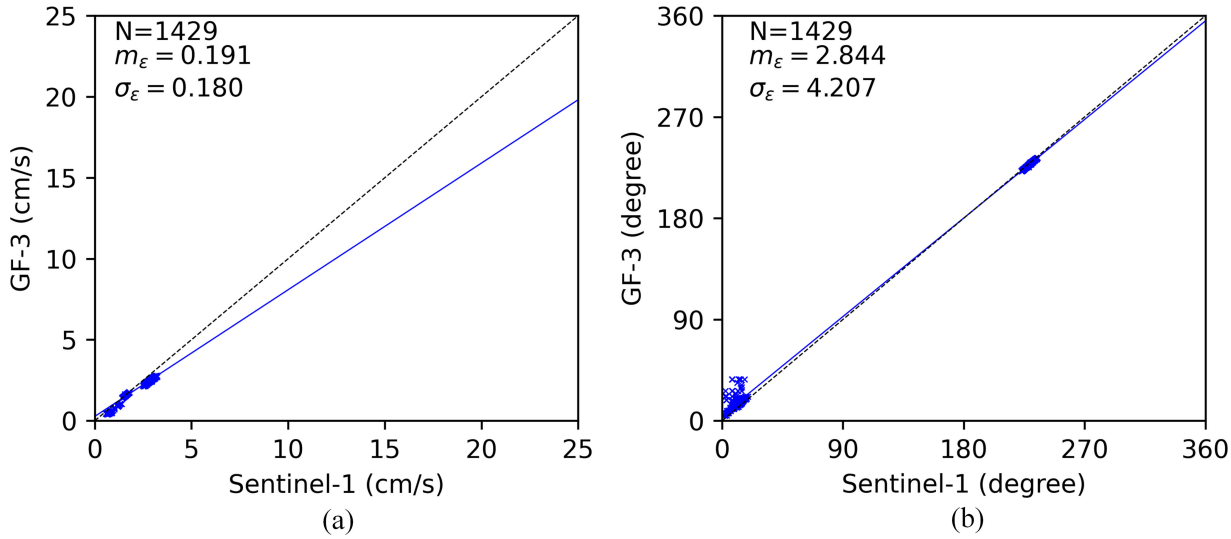

Fig. 16. Assessment of the accuracy of SIM vectors extracted from GF-3 images using SIM vectors extracted from Sentinel-1 images as reference data in terms of the (a) magnitude and (b) direction. The blue dashed line is a least-squares linear fit to the blue scatter points. N is the number of GF-3 and Sentinel-1 SIM vector pairs. m_ε and σ_ε are the mean and SD, respectively, of the absolute deviation of the magnitude or direction of the SIM vectors from GF-3 and Sentinel-1.

of extracting SIM vectors from GF-3 images was overestimated when using the manually extracted vectors as reference data. Based on the earlier, this article concludes that the uncertainty in the magnitude and direction of the SIM vectors extracted from GF-3 images using FT-MCC are 0.119 cm/s–0.287 cm/s (103 m/d–248 m/d) and 4.119°–5.930°, respectively.

V. Summary

In this article, a procedure for extracting SIM vectors from GF-3 imagery using the FT-MCC algorithm was presented. The effects of the spatial resolution and polarization mode of the GF-3 imagery on SIM vector extraction were discussed. The differences in the results and efficiency of SIM extraction from GF-3 images by FT(A-KAZE)-MCC and FT(ORB)-MCC methods are compared. Additionally, the accuracy of the SIM vectors extracted from GF-3 imagery was assessed.

We used LC flow field filtering to replace CCT filtering in FT-MCC to effectively eliminate erroneous SIM vectors, while retaining correct vectors with low correlation coefficients. Thus, the limitation of the CCT method, that is, the requirement of different thresholds for different scenarios, is eliminated and removal of erroneously extracted SIM vectors by FT-MCC is improved.

A comparison of the PDDs of the correlation coefficients of SIM vectors obtained from GF-3 images with different spatial resolutions showed that the reliability of SIM vectors obtained at 20 m resolution is poor for FSII mode images and better at 80 m

resolution. The ENLs of images with different spatial resolutions showed that high level of speckle noise in 20 m resolution FSII mode images reduced the reliability of SIM vector extraction at this resolution.

The polarization mode of an image also affected the reliability of the extracted SIM vectors. The reliability of SIM vectors extracted from VH-polarized images acquired in GF-3 FSII mode in the winter and summer was overall higher than from corresponding VV-polarized images. An analysis of the information entropy of different polarized images showed that the mean information entropy of VH-polarized images in winter and summer in FSII mode was than that of VV-polarized images. The larger the information entropy of the image, the richer the grayscale information in the image, which is more conducive to the extraction of SIM vectors with high reliability.

Extracting SIM vectors from GF-3 images using FT(A-KAZE)-MCC produced similar results at a significantly higher efficiency than using FT(ORB)-MCC. The use of different numbers of SIM vectors obtained through FT in the subsequent steps of the FT-MCC algorithm revealed that the FT-MCC algorithm was not sensitive to the number of SIM vectors obtained through FT when applied to GF-3 images, which further explained the high consistency between the results yielded by the FT(A-KAZE)-MCC and FT(ORB)-MCC algorithms.

The accuracy of SIM vector extraction by FT-MCC from GF-3 images was assessed using manually extracted SIM vectors and SIM vectors extracted from Sentinel-1 images as reference data. We also assessed SIM vector extracted from Sentinel-1 images using the CMEMS SIM product to demonstrate its reliability as reference data. The assessment results for SIM vectors extracted from the GF-3 image by FT-MCC using two independent reference data were used to calculate the SDs of the absolute differences in the magnitude and direction of the vectors as 0.119 cm/s–0.287 cm/s (103 m/d–248 m/d) and 4.119°–5.930°, respectively.

Due to the limitation of the coverage of GF-3 images in the Arctic and the winter and summer imaging modes, FSII mode winter and summer images were selected as experimental data to study of SIM data extraction from GF-3 images. The conclusions of this study are insufficient to assess the ability of FT-MCC to extract SIM vectors using GF-3 images across the entire Arctic. With the improvement in the coverage of the GF-3 satellite in the Arctic, GF-3 images for more areas will be employed to study SIM in the future.

ACKNOWLEDGMENT

The authors would like to thank the National Satellite Ocean Application Service for the GF-3 satellite data.

REFERENCES

[1] R. Kwok, "Arctic sea ice thickness, volume, and multiyear ice coverage: Losses and coupled variability (1958–2018)," *Environ. Res. Lett.*, vol. 13, no. 10, 2018, Art. no. 105005.

[2] G. Spreen, L. de Steur, D. Divine, S. Gerland, E. Hansen, and R. Kwok, "Arctic sea ice volume export through Fram Strait from 1992 to 2014," *J. Geophysical Res., Oceans*, vol. 125, no. 6, 2020, Art. no. e2019JC016039.

[3] L. H. Smedsrud, M. H. Halvorsen, J. C. Stroeve, R. Zhang, and K. Kloster, "Fram Strait sea ice export variability and September Arctic sea ice extent over the last 80 years," *Cryosphere*, vol. 11, no. 1, pp. 65–79, 2017.

[4] J. Wei, X. Zhang, and Z. Wang, "Reexamination of Fram Strait sea ice export and its role in recently accelerated Arctic sea ice retreat," *Climate Dyn.*, vol. 53, no. 3, pp. 1823–1841, 2019.

[5] T. Martin and E. Augstein, "Large-scale drift of Arctic sea ice retrieved from passive microwave satellite data," *J. Geophysical Res., Oceans*, vol. 105, no. C4, pp. 8775–8788, 2000.

[6] R. Kwok, "Summer sea ice motion from the 18 GHz channel of AMSR-E and the exchange of sea ice between the Pacific and Atlantic sectors," *Geophysical Res. Lett.*, vol. 35, no. 3, pp. 1–6, 2008.

[7] T. Lavergne, S. Eastwood, Z. Teffah, H. Schyberg, and L. A. Breivik, "Sea ice motion from low-resolution satellite sensors: An alternative method and its validation in the Arctic," *J. Geophysical Res., Ocean.*, vol. 115, no. 10, pp. 1–14, 2010.

[8] Z. I. Petrou and Y. L. Tian, "High-resolution sea ice motion estimation with optical flow using satellite spectroradiometer data," *IEEE Trans. Geosci. Remote Sens.*, vol. 55, no. 3, pp. 1339–1350, Mar. 2017.

[9] A. Liu, Y. Zhao, and S. Wu, "Arctic sea ice drift from wavelet analysis of NSCAT and special sensor microwave imager data," *J. Geophysical Res., Oceans*, vol. 104, pp. 529–538, 1999.

[10] W. J. Emery, C. W. Fowler, J. Hawkins, and R. H. Preller, "Fram Strait satellite image-derived ice motions," *J. Geophysical Res., Oceans*, vol. 96, no. C3, pp. 4751–4768, 1991.

[11] R. M. Ninnis, W. J. Emery, and M. J. Collins, "Automated extraction of pack ice motion from advanced very high resolution radiometer imagery," *J. Geophysical Res., Oceans*, vol. 91, no. C9, 1986, Art. no. 10725.

[12] R. Lopez-Acosta, M. P. Schodlok, and M. M. Wilhelmus, "Ice Floe Tracker: An algorithm to automatically retrieve Lagrangian trajectories via feature matching from moderate-resolution visual imagery," *Remote Sens. Environ.*, vol. 234, 2019, Art. no. 111406.

[13] W. Lang, Q. Wu, X. Zhang, J. Meng, N. Wang, and Y. Cao, "Sea ice drift tracking in the Bohai sea using geostationary ocean color imagery," *J. Appl. Remote Sens.*, vol. 8, Apr. 2014, Art. no. 83650.

[14] R. Wang, D. Huang, X. Zhang, and P. Wei, "Combined pattern matching and feature tracking for Bohai sea ice drift detection using Gaofen-4 imagery," *Int. J. Remote Sens.*, vol. 41, no. 19, pp. 7486–7508, Oct. 2020.

[15] R. Kwok, J. C. Curlander, R. McConnell, and S. S. Pang, "An ice-motion tracking system at the Alaska SAR facility," *IEEE J. Ocean. Eng.*, vol. 15, no. 1, pp. 44–54, Jan. 1990.

[16] M. Thomas, C. A. Geiger, and C. Kambhamettu, "High resolution (400 m) motion characterization of sea ice using ERS-1 SAR imagery," *Cold Regions Sci. Technol.*, vol. 52, no. 2, pp. 207–223, 2008.

[17] R. Kwok and D. Sulsky, "Arctic Ocean sea ice thickness and kinematics: Satellite retrievals and modeling," *Oceanography*, vol. 23, no. 4, pp. 134–143, 2010.

[18] J. Karvonen, "Operational SAR-based sea ice drift monitoring over the Baltic Sea," *Ocean Sci.*, vol. 8, no. 4, pp. 473–483, 2012.

[19] A. S. Komarov and D. G. Barber, "Sea ice motion tracking from sequential dual-polarization RADARSAT-2 images," *IEEE Trans. Geosci. Remote Sens.*, vol. 52, no. 1, pp. 121–136, Jan. 2014.

[20] X. Zhang, Y. Zhu, J. Zhang, J. Meng, X. Li, and X. Li, "An algorithm for sea ice drift retrieval based on trend of ice drift constraints from Sentinel-1 SAR data," *J. Coastal Res.*, vol. 102, no. sp1, pp. 113–126, Dec. 2020.

[21] R. Kwok, A. Schweiger, D. A. Rothrock, S. Pang, and C. Kottmeier, "Sea ice motion from satellite passive microwave imagery assessed with ERS SAR and buoy motions," *J. Geophysical Res., Oceans*, vol. 103, no. 3334, pp. 8191–8214, 1998.

[22] Y. Xian, Z. I. Petrou, Y. Tian, and W. N. Meier, "Super-resolved fine-scale sea ice motion tracking," *IEEE Trans. Geosci. Remote Sens.*, vol. 55, no. 10, pp. 5427–5439, Oct. 2017.

[23] J. Lehtiranta, S. Siiriä, and J. Karvonen, "Comparing C- and L-band SAR images for sea ice motion estimation," *Cryosphere*, vol. 9, no. 1, pp. 357–366, 2015.

[24] B. S. Reddy and B. N. Chatterji, "An FFT-based technique for translation, rotation, and scale-invariant image registration," *IEEE Trans. Image Process.*, vol. 5, no. 8, pp. 1266–1271, Aug. 1996.

[25] S. Muckenhuber, A. A. Korosov, and S. Sandven, "Open-source feature-tracking algorithm for sea ice drift retrieval from Sentinel-1 SAR imagery," *Cryosphere*, vol. 10, no. 2, pp. 913–925, 2016.

[26] D. Demchev, V. Volkov, E. Kazakov, P. F. Alcantarilla, S. Sandven, and V. Khmeleva, "Sea ice drift tracking from sequential SAR images using accelerated-KAZE features," *IEEE Trans. Geosci. Remote Sens.*, vol. 55, no. 9, pp. 5174–5184, Sep. 2017.

[27] S. Muckenhuber and S. Sandven, "Open-source sea ice drift algorithm for Sentinel-1 SAR imagery using a combination of feature tracking and pattern matching," *Cryosphere*, vol. 11, no. 4, pp. 1835–1850, 2017.

[28] A. A. Korosov and P. Rampal, "A combination of feature tracking and pattern matching with optimal parametrization for sea ice drift retrieval from SAR data," *Remote Sens.*, vol. 9, no. 3, 2017, Art. no. 258.
[29] J. W. Park *et al.*, "Feasibility study on estimation of sea ice drift from KOMPSAT-5 and COSMO-SkyMed SAR images," *Remote Sens.*, vol. 13, no. 20, pp. 1–15, 2021.
[30] V. Selyuzhenok and D. Demchev, "An application of sea ice tracking algorithm for fast ice and stamukhas detection in the arctic," *Remote Sens.*, vol. 13, no. 18, pp. 1–13, 2021.
[31] L. Li, Y. Zhu, J. Hong, F. Ming, and Y. Wang, "Design and implementation of a novel polarimetric active radar calibrator for Gaofen-3 SAR," *Sensors (Switzerland)*, vol. 18, no. 8, 2018, Art. no. 2620.
[32] H. Wang *et al.*, "Calibration of the copolarized backscattering measurements from Gaofen-3 synthetic aperture radar wave mode imagery," *IEEE J. Sel. Topics Appl. Earth Observ. Remote Sens.*, vol. 12, no. 6, pp. 1748–1762, Jun. 2019.
[33] R. Zhao, G. Zhang, M. Deng, K. Xu, and F. Guo, "Geometric calibration and accuracy verification of the GF-3 satellite," *Sensors (Switzerland)*, vol. 17, no. 9, 2017, Art. no. 1977.
[34] Y. Wang, C. Wang, H. Zhang, Y. Dong, and S. Wei, "Automatic ship detection based on RetinaNet using multi-resolution Gaofen-3 imagery," *Remote Sens.*, vol. 11, no. 5, pp. 1–14, 2019.
[35] X. M. Li, T. Zhang, B. Huang, and T. Jia, "Capabilities of Chinese Gaofen-3 synthetic aperture radar in selected topics for coastal and ocean observations," *Remote Sens.*, vol. 10, no. 12, 2018, Art. no. 1929.
[36] H. Wang *et al.*, "GF-3 SAR ocean wind retrieval: The first view and preliminary assessment," *Remote Sens.*, vol. 9, no. 7, pp. 1–12, 2017.
[37] J. Li, C. Wang, S. Wang, H. Zhang, Q. Fu, and Y. Wang, "Gaofen-3 sea ice detection based on deep learning," in *Proc. Prog. Electromagn. Res. Symp.*, 2017, pp. 933–939.
[38] T. Zhang *et al.*, "Deep learning based sea ice classification with Gaofen-3 fully polarimetric SAR data," *Remote Sens.*, vol. 13, no. 8, 2021, Art. no. 1452.
[39] A. M. Johansson and A. Berg, "Agreement and complementarity of sea ice drift products," *IEEE J. Sel. Topics Appl. Earth Observ. Remote Sens.*, vol. 9, no. 1, pp. 369–380, Jan. 2016.
[40] H. Sumata *et al.*, "An intercomparison of Arctic ice drift products to deduce uncertainty estimates," *J. Geophysical Res., Oceans*, vol. 119, pp. 4887–4921, 2014.
[41] L. T. Pedersen, R. Saldo, and R. Fenger-Nielsen, "Sentinel-1 results: Sea ice operational monitoring," in *Proc. IEEE Int. Geosci. Remote Sens. Symp.*, 2015, pp. 2828–2831.
[42] J.-S. Lee, "Digital image enhancement and noise filtering by use of local statistics," *IEEE Trans. Pattern Anal. Mach. Intell.*, vol. PAMI-2, no. 2, pp. 165–168, Mar. 1980.
[43] T. Lavergne, "Algorithm theoretical basis document for OSI SAF medium resolution sea ice drift product," Version 1.3, 2016.
[44] C. E. Shannon, "A mathematical theory of communication," *Bell Syst. Tech. J.*, vol. 27, no. 3, pp. 379–423, 623–656, 1948.
[45] X. Y. Liu *et al.*, "Quality assessment of speckle patterns for digital image correlation by Shannon entropy," *Optik (Stuttg)*, vol. 126, no. 23, pp. 4206–4211, 2015.
[46] L. H. Smedsrud, A. Sirevaag, K. Kloster, A. Sorteberg, and S. Sandven, "Recent wind driven high sea ice area export in the Fram Strait contributes to Arctic sea ice decline," *Cryosphere*, vol. 5, pp. 821–829, 2011.
[47] P. R. Bevington and D. K. Robinson, *Data Reduction and Error Analysis for the Physical Sciences*, 3rd ed. New York, NY, USA: McGraw-Hill, 2003.

Mingci Li received the B.S. degree in surveying and mapping engineering from the North China University of Water Resources and Electric Power, Zhengzhou, China, in 2012, and the M.S. degree in geodesy and geomatics engineering from the Beijing University of Civil Engineering and Architecture, Beijing, China, in 2015. He is currently working toward the Ph.D. degree in photogrammetry and remote sensing with the Chinese Antarctic Center of Surveying and Mapping, Wuhan University, Wuhan, China.

His research interests include polar remote sensing, sea ice kinematic, and information extraction from SAR images.

Chunxia Zhou received the B.S. and M.S. degrees in geodesy and geomatics from the Wuhan Technical University of Surveying and Mapping, Wuhan, China, in 1998 and 2000, respectively, and the Ph.D. degree in solid earth geophysics from Wuhan University, Wuhan, China, in 2005.

She is currently a Professor with the Chinese Antarctic Center of Surveying and Mapping, Wuhan University. She has participated in fieldwork in Antarctica and Svalbard. Her research interests include SAR interferometry, polar remote sensing, and global environmental change.

Bing Li received the B.S. degree from the Chengdu University of Technology, Chengdu, China, in 2015, and the Ph.D. degree from the Chinese Antarctic Center of Surveying and Mapping, Wuhan University, Wuhan, China, in 2021.

He is currently a Lecturer with the School of Mathematics and Computer Science, Wuhan Polytechnic University, Wuhan, China. His main research interests focus on the estimation and compensation of ionospheric propagation delay in Synthetic Aperture Radar Interferometry (InSAR) and polar remote sensing.

Xiaoli Chen received the B.S. degree in geographical information science from Zhengzhou University, Zhengzhou, China, in 2019. She is currently working toward the M.S. degree in photogrammetry and remote sensing with the Chinese Antarctic Center of Surveying and Mapping, Wuhan University, Wuhan, China.

Her research interests include polar remote sensing, arctic sea ice, surface melting, melt ponds, and sea ice phenology.

Jianqiang Liu received the B.S. degree in geophysics from Peking University, Beijing, China, in 1986, and the master's degree in marine meteorology from the National Marine Environmental Forecasting Center, State Oceanic Administration, Beijing, China, in 1989.

He is currently with the National Satellite Ocean Application Service, Beijing, China. He is the Chief Designer of the ground application system with the Chinese–France Ocean satellite and new generational ocean color satellites. He was a Deputy Chief Designer of the ground application system for the HY-1 and HY-2 satellites. He is one of the founders of satellite ocean remote sensing in China and plays an important role in the development of Chinese ocean satellites and manned space flight. His research interests include ocean color and sea wave satellite data processing, applications of ocean remote sensing data, and Antarctic research.

Tao Zeng received the B.S. degree from the School of Remote Sensing and Information Engineering, Wuhan University, Wuhan, China, in 2003, and the M.S. degree in marine remote sensing from the National Marine Environmental Forecasting Center, State Oceanic Administration, Beijing, China, in 2006.

He works with the Department of Polar Remote Sensing, National Satellite Ocean Application Service, Beijing, China. His research mainly focuses on satellite image processing and sea ice remote sensing.